PAPER

Check for updates

How to efficiently isolate multiple size ranges of oxidized or hydrogenated milled nanodiamonds†

Marie Finas, Hugues A. Girard [ID] and Jean-Charles Arnault [ID] *

Nanodiamonds exhibit various properties, such as surface reconstruction, electrostatic potentials of facets, and thermal, fluorescence, or quantum characteristics, which are dependent on their size. However, the synthesis method can lead to significant size polydispersity, particularly in nanodiamonds obtained from milling (MND). Therefore, it is essential to efficiently sort MND by size to ensure uniformity and optimize their properties for biomedical, sensing or energy applications. This method successfully isolates nanodiamonds into three distinct size ranges: approximately 10 nm for the smallest, 25 nm for the intermediate, and 35 nm for the largest. The protocol was then extended to hydrogenated MND from the same source, resulting in the separation of similar size populations.

1. Introduction

Diamond nanoparticles, commonly referred to as nanodiamonds (ND), are currently under extensive investigation in various application fields such as nanomedicine,[1] photo(electro)catalysis,[2] quantum sensors,[3] advanced lubricants and composites.[4] These applications involve different types of nanodiamonds, some milled from bulk HPHT, CVD, or natural diamond (MND), and others synthesized by detonation (DND), each exhibiting distinct characteristics.[5] MND, typically sized in the tens of nanometers, possess an excellent crystalline quality that results in optical and electronic properties closely resembling those of bulk diamond.[6,7] Conversely, milled and detonation nanodiamonds significantly differ in shape (facetted or rounded) and in the nature and concentration of impurities hosted in the diamond lattice.[8,9] A recent comparison between MND and DND of a few nanometers has underscored these differences.[10] Consequently, each type of ND is preferably used for specific applications. For instance, MND, with their spin properties imparted by color centers, are considered in quantum applications like temperature sensors,[11] whereas the nanometric size of DND is advantageous for their clearance in drug delivery applications.[12]

MND exhibit a high polydispersity in size and in shape, which has been nicely evidenced in a previous TEM investigation that revealed that the size distribution of MND said to range from 0 to 50 nm was highly concentrated in particles smaller than 10 nm.[13] However, the ND size strongly affects the surface and bulk properties. At the surface, reconstruction occurs depending on the curvature and the facet nature.[14] As an example, fullerene-like shells exhibiting high convexity were predicted and observed for ND smaller than 3 nm.[15,16] The presence of sp^2 carbon at the surface can severely affect the ND thermal conductivity.[17] Such surface reconstruction also induces a strain relaxation within the ND core. In addition, ND size affects the nature of facets that play a critical role in the distribution of surface electrostatic potential on ND.[18] Consequently, the colloidal properties of ND will strongly depend on their size. Properties of hydrogenated MND like negative electron affinity and surface conductivity are also highly dependent on their size according to a recent report.[19] Among bulk assets, the thermal diffusivity is strongly affected at the nanoscale as shown by experiments and calculations.[20] For ND smaller than 2–3 nm, depending on their shape, a quantum confinement occurs leading to an increased band gap.[21,22] Increasing ND size leads to higher density of NV centers in their core resulting in brighter fluorescence. For all these reasons, having monodisperse particles of high crystalline quality such as MND to work with is particularly desirable.

Bottom-up approaches to grow tailored nanodiamonds either by HPHT or CVD synthesis have recently emerged.[23,24] Nevertheless, these approaches are not mature enough to provide a durable source of ND. An alternative would consist in fractioning an initial polydisperse ND suspension into a stable and monodisperse colloid. For nanoparticles in general, various post-synthesis treatments were reported to separate them in size. They include membrane filtration, chromatography, electrophoresis and magnetic separation.[25] However, these techniques require specific equipment, adapted sample preparation and specific properties. Focusing on nanodiamonds, centrifugation, known for its simplicity, speed and cost-effectiveness, was used in various studies. Initially, ultracentrifugation was employed to isolate ultra-small (<4 nm) MND for comparative

Université Paris-Saclay, CEA, CNRS, NIMBE, 91191 Gif sur Yvette, France. E-mail: jean-charles.arnault@cea.fr

† Electronic supplementary information (ESI) available. See DOI: https://doi.org/10.1039/d4na00487f

analysis with DND.[26] Conversely, it allows an elimination of aggregates from a DND suspension through centrifugation, ensuring stability of only 4–6 nm ND in suspension.[27] Ultracentrifugation has emerged as a viable technique for isolating small ND sizes but lacks efficiency in fractionating into distinct size ranges.

To isolate multiple size ranges, a coupling between centrifugation and a density gradient demonstrated its efficiency. This approach also offers scalability and prevents NP agglomeration. By implementing a density gradient in a tube and selecting appropriate centrifugation conditions, NP are efficiently separated based on their mass and consequently their size. A previous study implemented a PVP gradient to sort Au and iron oxide NP, noting that a viscosity gradient is more effective than a density gradient for separating large NP.[28] Another investigation demonstrated that a high viscosity gradient can effectively separate metallic NP like Ag and Au based on their size, composition and surface chemistry.[29] Non-uniform shaped and mixed core-composition NP can be fractionated using a step gradient of sucrose.[30] Similarly, a sucrose gradient was used to separate silver NP coated with chitosan.[31] While a density gradient coupled with centrifugation proves effective for separating NP based on size or composition, a viscosity gradient is more suitable for isolating large NP. As diamond density (3.5 g cm^{-3}) is greater than the density of an aqueous mixture, nanodiamonds cannot reach a density equilibrium in the medium and their fractionation is referred to as rate-zonal separation (RZS). Under these conditions, centrifugation time and speed should be carefully chosen to prevent all ND from migrating to the bottom of the container. In that way, MND and DND were sorted using density gradient ultracentrifugation with short centrifugation time and high speed.[32,33] Under specific conditions, this approach even allowed the fractionation of hundreds of milligrams of ND.[33] Nevertheless, if DND with different surface chemistries were fractionated using a PVP gradient,[34] a parametric study focused on the MND sorting in several size ranges and different surface chemistries is still lacking.

In the present study, we propose to isolate a new, larger range of ND sizes whose surface properties will be studied and compared to smaller ND. An aqueous ethylene glycol (EG) step gradient was used to fractionate oxidized HPHT milled ND in size. The influence of the starting material and the role of centrifugation parameters on size sorting efficiency are accurately studied. Once sorted, MND were characterized using DLS, SEM, UV-vis and FTIR spectroscopies. A compromise between the amount of collected MND and sorting efficiency needs to be found. We also show that such an approach can be applied in the same way to both oxidized and hydrogenated particles.

2. Results

2.1 Methodology to estimate the size distribution of a polydisperse population

Estimating the polydispersity of an NP suspension using standard laboratory methods remains a challenge. The most common technique for assessing the size distribution of suspended objects is dynamic light scattering (DLS). However, if this technique is very effective for monodisperse and spherical particles, the shape anisotropy and polydispersity of milled nanodiamonds (MND) can interfere with the measurements. In addition, DLS cannot distinguish an aggregate from a single particle if they have the same hydrodynamic diameter. Therefore, to estimate the real dimensions of MND (at least their Feret diameter), a direct observation by electron microscopy is mandatory (scanning or transmission modes). For this purpose, drop-cast deposition of MND on a flat substrate or on a TEM grid would normally be used. However, this method of deposition generally results in strong aggregation of NP upon drying, which prevents them from being measured individually (Fig. S1†). To overcome this limitation, we propose here a layer-by-layer approach. Driven by electrostatic interactions, this approach allows the deposition of ND on substrates of very different shapes.[35,36] In addition, this technique produces a reproducible monolayer of nanoparticles that are isolated from each other, allowing optimal visualization by SEM or TEM (Fig. S1†).[13]

In order to ascertain the relative merits and shortcomings of these two methodologies (DLS and SEM observation) in estimating the polydispersity of an MND suspension, we initially observed three sets of HPHT-milled nanodiamonds exhibiting varying maximum diameters in accordance with the manufacturer's specifications. We used SYP 0–0.03 nanodiamonds, which range from 0 to 30 nm, SYP 0–0.05 from 0 to 50 nm and SYP 0–0.1 from 0 to 100 nm. Each set of MND was dispersed in aqueous suspension *via* sonication and centrifugation steps. Carboxylic groups at the surface of the different MND confer on them negative zeta potentials (*ca.* −40 mV at pH = 6) high enough to ensure a colloidal stability, enabling confidence measurements by DLS and optimized layer-by-layer deposition. Fig. 1 (left) reports on the proportions of NP according to their hydrodynamic diameter as measured by DLS. These distributions show significant differences between the three sets of MND with a mean hydrodynamic diameter of 21 nm for SYP 0–0.03, 25 nm for SYP 0–0.05 and 29 nm for SYP 0–0.1. DLS also evidences that there are smaller objects (<20 nm) in the SYP 0–0.03 while larger objects (>30 nm) are mostly detected in SYP 50 and SYP 100. However, as explained earlier, these large objects can be single MND of large diameter or assemblies of small MND. In addition, it should be noted that this DLS measurement seems to indicate that there are no NP < 10 nm in SYP 0–0.03 and < 20 nm in SYP 0–0.1. Finally, polydispersity indexes (PDI) given by the DLS measurements evidence a moderately broad size distribution (0.08 <PDI <0.7).[37]

Size distributions of these three sets of commercial MND were then determined *via* analysis of the FEG-SEM pictures (see the methodology in the experimental). Unlike DLS measurements, distributions of Feret diameters, displayed in Fig. 1 (right), appear fairly similar for the three samples, with equivalent mean diameters. Differences arise only for the smallest nanoparticles (<10 nm), which were invisible in DLS representations. On the other hand, the differences between the three sets in terms of the largest nanoparticles (>20 nm) are much less marked than reported by DLS. This may be due either to the

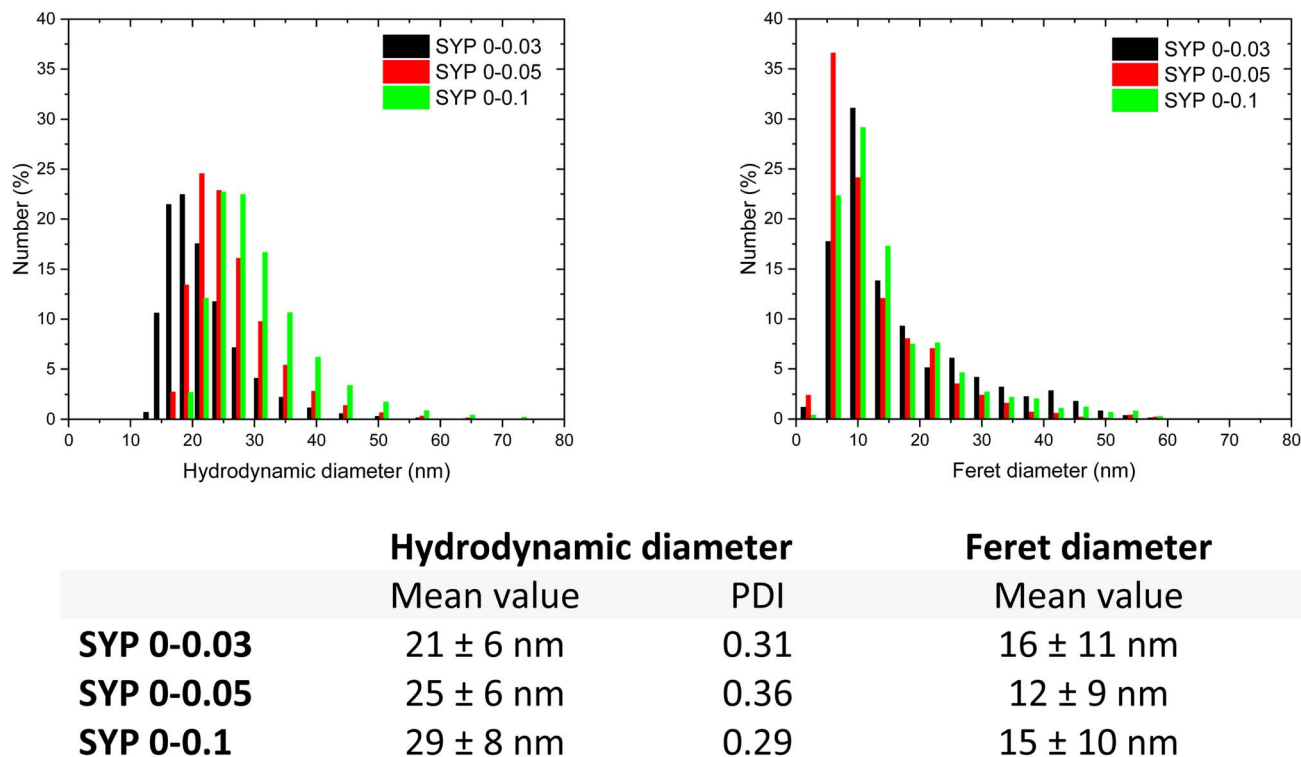| | **Hydrodynamic diameter** | | **Feret diameter** |
	Mean value	PDI	Mean value
SYP 0-0.03	21 ± 6 nm	0.31	16 ± 11 nm
SYP 0-0.05	25 ± 6 nm	0.36	12 ± 9 nm
SYP 0-0.1	29 ± 8 nm	0.29	15 ± 10 nm

Fig. 1 For the first three MND sets: (top left) distributions of hydrodynamic diameters obtained by DLS, the concentration of MND in a water suspension is 0.5 mg mL; (top right) distributions of Feret diameters extracted from FEG–SEM image analysis; (bottom) table of the mean diameters and PDI. Statistics of counted MND is provided in the ESI (see Table S1†).

presence of aggregates in the colloids, seen by the DLS, which are not transferred to the monolayer, or to the difficulty of the DLS in handling such a polydisperse sample. This last point will be discussed in the last part of this manuscript. Nevertheless, the combination of these two techniques appears to offer a satisfactory compromise for the assessment of polydispersity in a suspension. One technique is able of highlighting larger objects, while the other is more sensitive to the smallest.

For the rest of the study, we choose SYP 0–0.1 nanoparticles to extend the range of diameters to be separated as far as possible. SYP 0–0.1 MND were oxidized under air annealing to efficiently remove the residual non-diamond carbon from the MND surface and promote carbon/oxygen functional groups (see the oxidation parameters in the experimental section).

2.2 Size sorting of oxidized MND

Having now defined the observation techniques that will enable us to better characterize the MND polydispersity, the method used for size sorting of MND-Ox can now be detailed. Here, we used a viscosity gradient combined with centrifugation (Fig. S2†). The viscosity gradient was obtained by superimposing phases containing a mixture of H_2O/EG in different proportions (see the experimental part for more details on the gradient). Preliminary experiments enabled us to define that a superposition of phases with 10 to 60% EG in water, with increments of 10%, was the most suitable. These preliminary experiments also established that MND-Ox were stable in the H_2O/EG mixture whatever the proportion of EG. After centrifugation, the different phases are collected and to preserve their colloidal stability, we opted for purification of the EG by dialysis rather than a conventional centrifugation/redispersion cycle, which would have reintroduced aggregation. A flowchart of the protocol is shown in Fig. 2. DLS measurements and layer-by-layer deposition were therefore carried out at the end of the dialysis. Concentrations of MND collected in each phase were estimated from UV-vis spectra (see details in the experimental part).
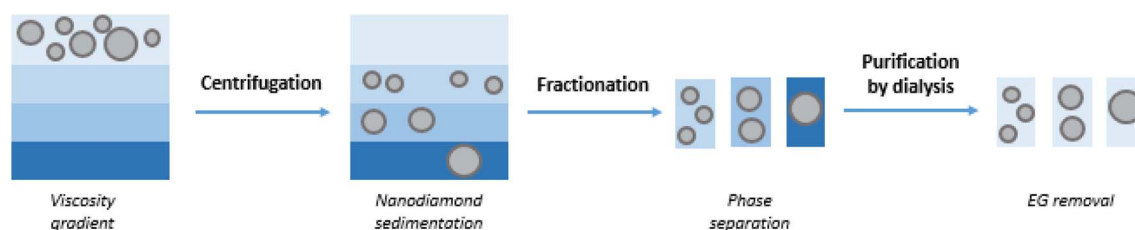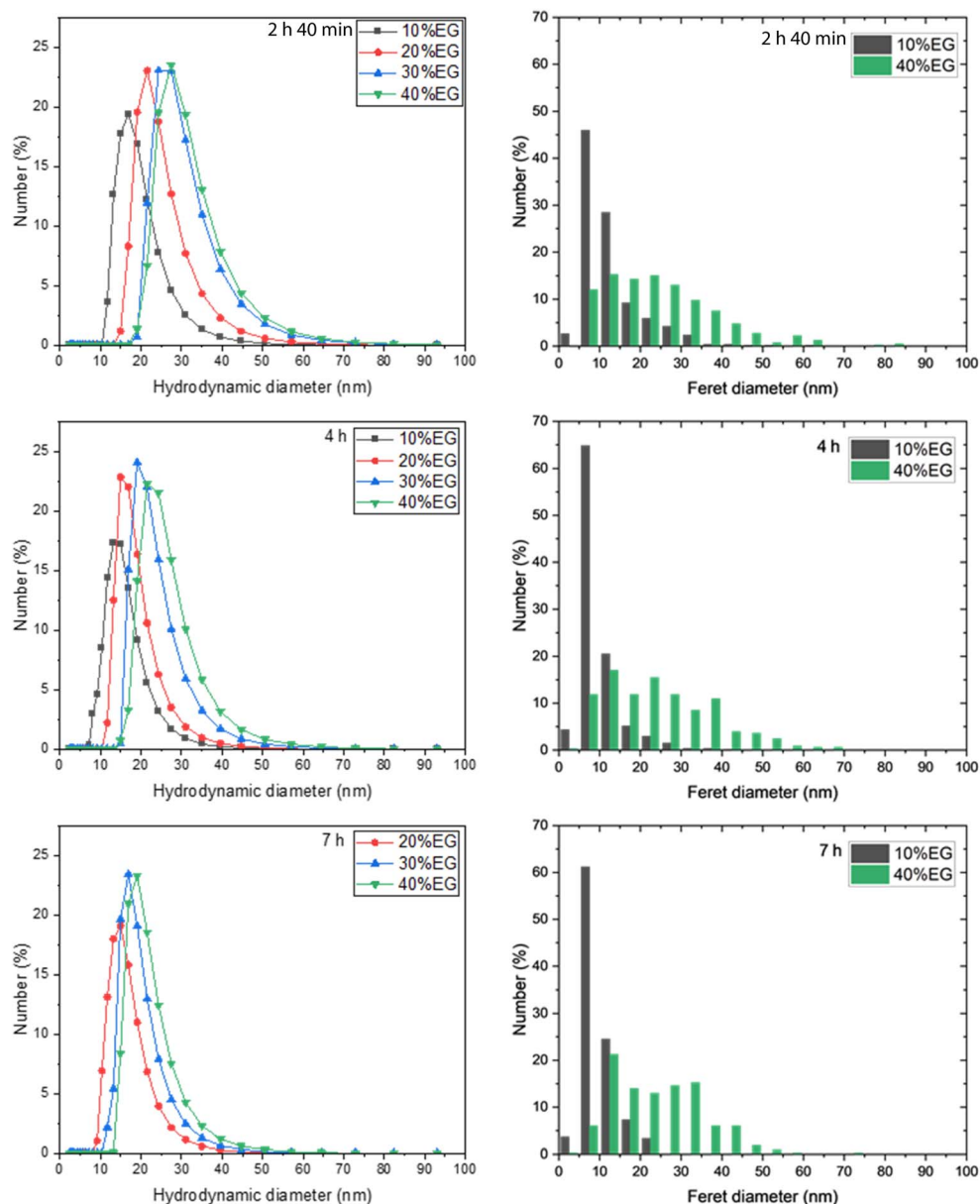

Fig. 2 Flowchart of the nanodiamond size sorting protocol.

		Hydrodynamic diameter		**Feret diameter**
		Mean value	PDI	Mean value
2h40	10% EG	19 ± 6 nm	0.36	12 ± 7 nm
	40% EG	31 ± 8 nm	0.23	25 ± 14 nm
4h	10% EG	15 ± 5 nm	0.36	10 ± 5 nm
	40% EG	26 ± 7 nm	0.28	25 ± 13 nm
7h	20% EG	19 ± 5 nm	0.37	10 ± 4 nm
	40% EG	21 ± 6 nm	0.29	24 ± 11 nm

Fig. 3 Size sorting of Ox-MND (SYP 0−0.1) in a % EG/water viscosity gradient: influence of the centrifugation time (2 h 40 min to 7 h); the centrifugation speed is 2400*g*. (Top left) Distributions of hydrodynamic diameters obtained by DLS for the first four different % EG/water layers; (top right) distributions of Feret diameters obtained by SEM image analysis for 10% and 40% EG layers (see pictures in Fig. S3†); (bottom) table of the mean diameters and PDI. Statistics of counted MND are provided in Table S1.†

2.2.1 Influence of the centrifugation duration. After 2 h 40 min of centrifugation at a speed of 2400g, Ox-MND fractions collected within the first four % EG/water layers (10% EG to 40% EG) and purified by dialysis exhibited an excellent colloidal stability. They also revealed separated distributions for hydrodynamic diameters (Fig. 3, left column). The maximum of distribution is centered at 19 nm for 10% EG, while it locates at 22 nm for 20% EG and 24 nm and 31 nm for 30% EG and 40% EG (Table 1). The same trend is observed when looking at the mean diameters, which is associated with an apparent decrease in the polydispersity index (Fig. 3, bottom). Note that the 50% and 60% EG phases contained almost no MND whatever the centrifugation conditions, hence they do not appear in the measurements reported here. The representative SEM images for Ox-MND collected from 10% EG and 40% EG after adsorption on PDDAC are provided in Fig. S3.† The corresponding distributions of Feret diameters (Fig. 3, right column) reveal two different populations: one sharp size distribution with 90% of Ox-MND between 10 and 15 nm (mean value 12 ± 7 nm) originating from the 10% EG layer, and a broader one with larger nanoparticles (from 10 nm up to 50 nm, mean value of 25 ± 14 nm) for the 40% EG. Note that small MND are still visible in the FEG-SEM picture for 40% EG (Fig. S3†). Here, the combination of the two techniques provides a higher degree of confidence in the observed results.

When the centrifugation time is extended to 4 h, hydrodynamic diameters (most prevalent diameters and mean values) appear slightly weaker between EG/water layers (Fig. 3 and Table 1). As with the 2 h 40 min centrifugation, a decrease in PDI is observed in the 40% phase compared to the 10% phase, which tends to indicate a lower polydispersity as small particles are eliminated. Size distributions extracted from FEG-SEM pictures evidence a similar size selection for the 40% EG layer compared to the shorter centrifugation (2 h 40 min), and a higher fraction of small nanoparticles in the 10% EG layer: 77% of ND are smaller than 15 nm in the 10% EG layer for 2 h 40 min centrifugation and 90% in the same layer for 4 h. In the meantime, the smallest nanoparticles that were visible on the SEM images of the 40% fractions after 2 h 40 min have now disappeared (Fig. S3†). For a longer centrifugation (7 h), size shrinking continues according to DLS (concentration in the 10% EG layer became too weak for proper DLS measurement, see the experimental part) (Fig. 3 and Table 1). The counting from FEG-SEM pictures reveals a size sorting comparable to the intermediate duration (4 h).

The three samples were also compared in terms of recovered amounts of Ox-MND in each gradient layer (Table 2). As expected, the centrifugation time affects the total quantity of

Table 2 Percentages of recovered Ox-MND for each gradient layer for different centrifugation durations at 2400g

	2 h 40 min	4 h	7 h
10% EG	7.5%	5.5%	1.8%
20% EG	11.6%	8.3%	4.1%
30% EG	9.6%	9.7%	5.7%
40% EG	5.1%	7.8%	6.0%
Total	33.8%	31.3%	17.6%

Table 3 Percentages of recovered Ox-MND for each gradient layer for different centrifugation speeds with similar duration (4 h)

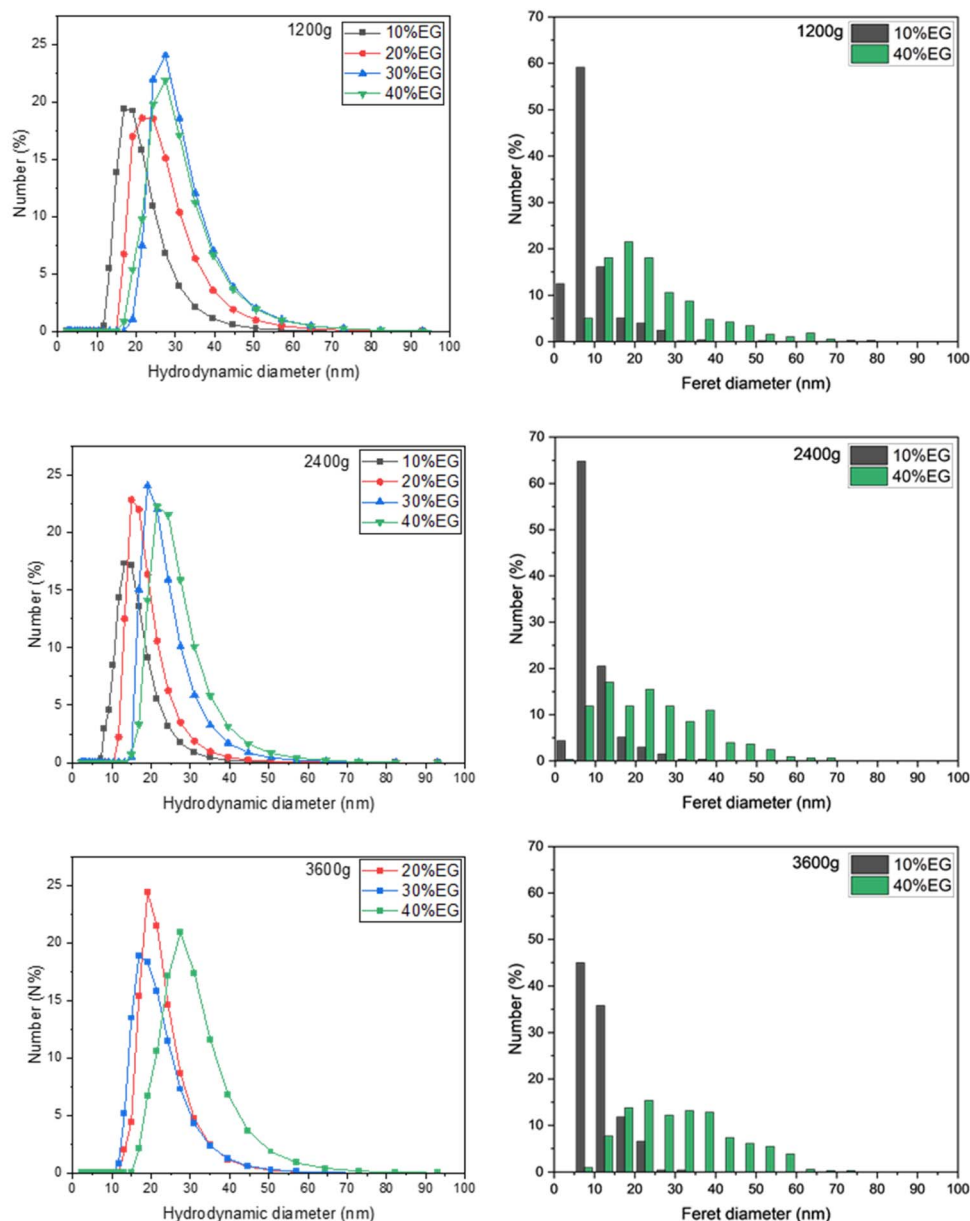|	1200g	2400g	3600g
10% EG	12.7%	5.5%	2.3%
20% EG	18.6%	8.3%	4.9%
30% EG	17.1%	9.7%	5.1%
40% EG	5.0%	7.8%	4.4%
Total	53.4%	31.3%	16.7%

nanoparticles recovered in the phases, which drop down to less than 20% of the initial mass after 7 h. It can also be seen that the duration of centrifugation influences which phase will be the most concentrated. The 20%, 30% and 40% phases are the most concentrated in MND for centrifugation times of 2 h 40 min, 4 h and 7 h, respectively. Considering all these results, a centrifugation duration of 4 h was selected to further investigate the effect of the centrifugation speed on the size sorting.

2.2.2 Influence of the centrifugation speed. At 1200g for 4 h, Ox-MND well separated in size within 10% EG and 40% EG as shown by both DLS and SEM counting (Fig. 4, left and right columns). The majority of Ox-MND exhibit sizes around 10–15 nm and 15–55 nm, for 10% EG and 40% EG, respectively. The maxima of distribution of hydrodynamic diameters are 17, 22, 27 and 27 nm moving from 10% to 40% EG gradient layers (Table 1). When the centrifugation speed is increased from 1200g to 3600g, the size sorting given by SEM measurement remains similar, with very close distributions of Feret diameter: one sharp size distribution centered at 10–15 nm for 10% EG, and a broad one within 15–55 nm for 40% EG. Corresponding FEG-SEM pictures are provided in Fig. S4.† Here as well, polydispersity appears lower in 40% EG layers compared to 10% EG layers. However, for the faster centrifugation, the increase in centrifugal force drastically reduces the amount of nanoparticles present in the 10% phase: only 2.3% of the initial mass is collected in the 10% EG phase and 4.4% in the 40% EG phase. According to our experiments, the better compromise for size sorting of Ox-MND corresponds to a centrifugation step performed at 2400g during 4 h.

2.3 Size sorting upscaling

In order to further increase the amount of collected size sorted Ox-MND, the tube dimension was enlarged from a volume of 15 mL to 50 mL. Centrifugation parameters previously selected were applied, *i. e.* 2400g during 4 h. The viscosity gradient was adapted to this larger tube to reach similar phase heights to ensure a comparable Ox-MND behavior during the size sorting.

Table 1 Most prevalent hydrodynamic diameters obtained by DLS for each gradient layer *versus* centrifugation duration and speed

Duration	Speed	10% EG	20% EG	30% EG	40% EG
2 h 40 min	2400g	17 nm	22 nm	24 nm	27 nm
4 h	2400g	13 nm	15 nm	19 nm	22 nm
7 h	2400g	—	15 nm	17 nm	19 nm
4 h	1200g	17 nm	22 nm	27 nm	27 nm
4 h	3600g	—	19 nm	19 nm	27 nm

		Hydrodynamic diameter		Feret diameter
		Mean value	PDI	Mean value
1200g	10% EG	21 ± 6 nm	0.38	10 ± 6 nm
	40% EG	30 ± 15 nm	0.31	25 ± 13 nm
2400g	10% EG	15 ± 5 nm	0.36	10 ± 5 nm
	40% EG	26 ± 7 nm	0.28	25 ± 13 nm
3600g	20% EG	21 ± 6 nm	0.38	12 ± 5 nm
	40% EG	29 ± 8 nm	0.33	31 ± 13 nm

Fig. 4 Size sorting of oxidized SYP 0–0.1 nanodiamonds in a % EG/water viscosity gradient: influence of the centrifugation speed (1200*g* to 3600*g*); the centrifugation duration is 4 h. (Top left) Distributions of hydrodynamic diameters obtained by DLS for the first four EG/water layers; (top right) distributions of Feret diameters obtained by SEM image analysis for 10% and 40% EG layers. (Bottom) Table of the mean diameters and PDI. Statistics of counted MND are provided in the ESI.†
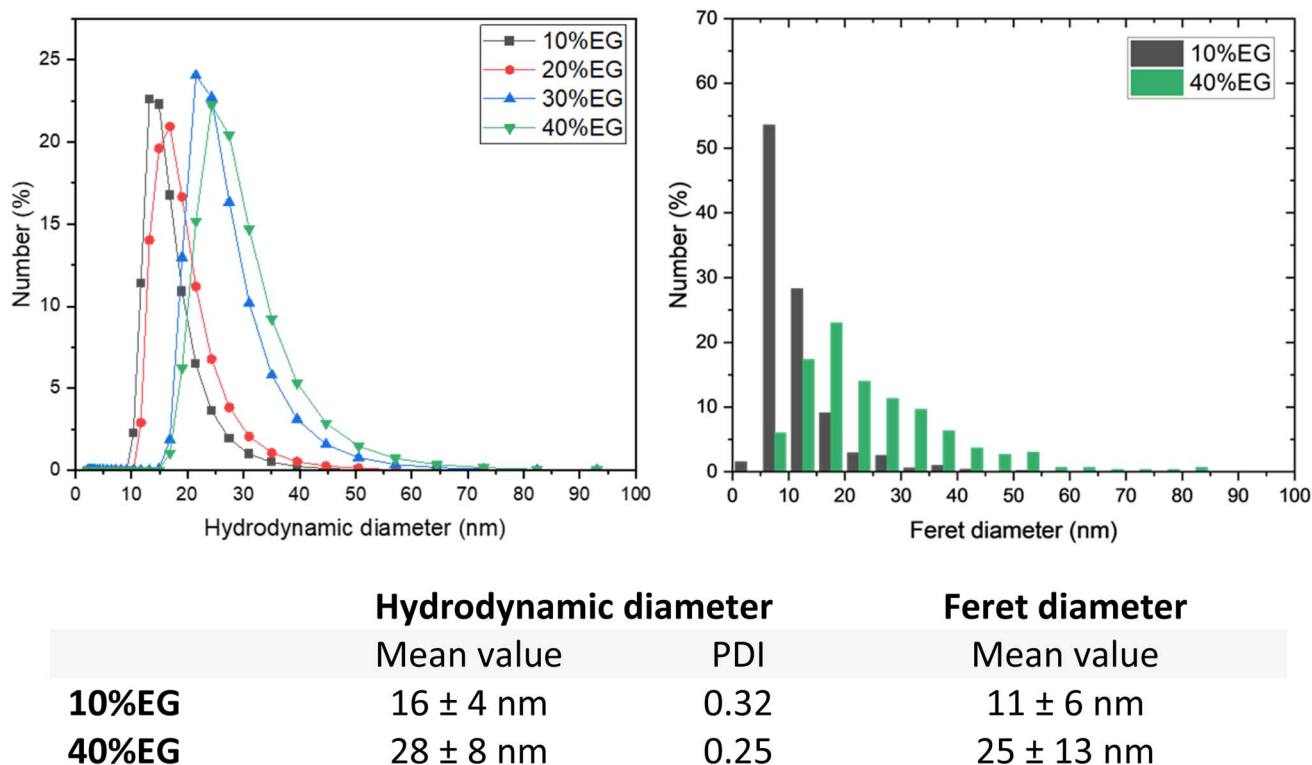

	Hydrodynamic diameter		Feret diameter
	Mean value	PDI	Mean value
10%EG	16 ± 4 nm	0.32	11 ± 6 nm
40%EG	28 ± 8 nm	0.25	25 ± 13 nm

Fig. 5 Size distributions extracted from DLS (left) and SEM pictures (right) of Ox-MND collected within 10% EG and 40% in the larger tube; (bottom) table of the mean diameters and PDI.

Size distributions of Ox-MND collected from 10% EG and 40% EG layers, extracted from DLS and FEG-SEM counting, are compared in Fig. 5. Results look very similar to those obtained with a smaller tube, with a sharp size distribution centered at 10–15 nm for the 10% EG and a broad size distribution from 15 to 55 nm for 40% EG.

Table 4 reports on the collected mass for each tube. The use of the larger one leads to a usable amount of size sorted Ox-MND: 1 mg for the smallest, and close to 3 mg for the largest. It corresponds to a slightly higher percentage of the initial mass, roughly 10% in the 40% EG layer. It retains 5% of the initial mass in the 10% EG layer.

2.4 Characterization of the tube pellet

Table 4 also shows that over 60% of the initial mass is not collected in the phases ranging from 10% to 40%. Excluding the

phase at 50% and 60%, which contains a negligible amount of Ox-MND, this highlights that all these NP end up in the centrifugation tube pellet. To determine whether this pellet is representative of the initial suspension or if sorting has also occurred within it, we characterized it in the same manner as the intermediate phases. The DLS characterization and a typical SEM picture of the Ox-MND collected in the sediment of the small tube are displayed in Fig. 6. The comparison with the data of the different gradient layers (EG 10% to EG 40%) emphasizes a distribution of hydrodynamic diameters located at larger sizes with a mean value at 35 nm and a PDI reduced to 0.23, one of the lowest values obtained so far. The SEM image of Ox-MND from the sediment adsorbed on PDDAC coating confirms the presence of large MND. After image analysis, the size distribution is located between 20 and 55 nm. Smallest Ox-MND (<15 nm) are not present in the centrifugation tube pellet.

3. Discussion

3.1 Size sorting

In this study, we demonstrated that the use of a viscosity gradient can isolate diameter ranges from a typical polydisperse MND solution. It appeared that the centrifugation speed and its duration are parameters to be taken into account, both for the size sorting aspect and in terms of the quantity of particles sorted. As shown by SEM pictures and size distributions from counting, a large number of small Ox-MND are collected in the first gradient layer (10% EG). However, this numerous population only represents 5% of the initial mass whatever the tube

Table 4 Collected masses in mg and as percentages of the initial mass in the first four EG/water layers for both tubes

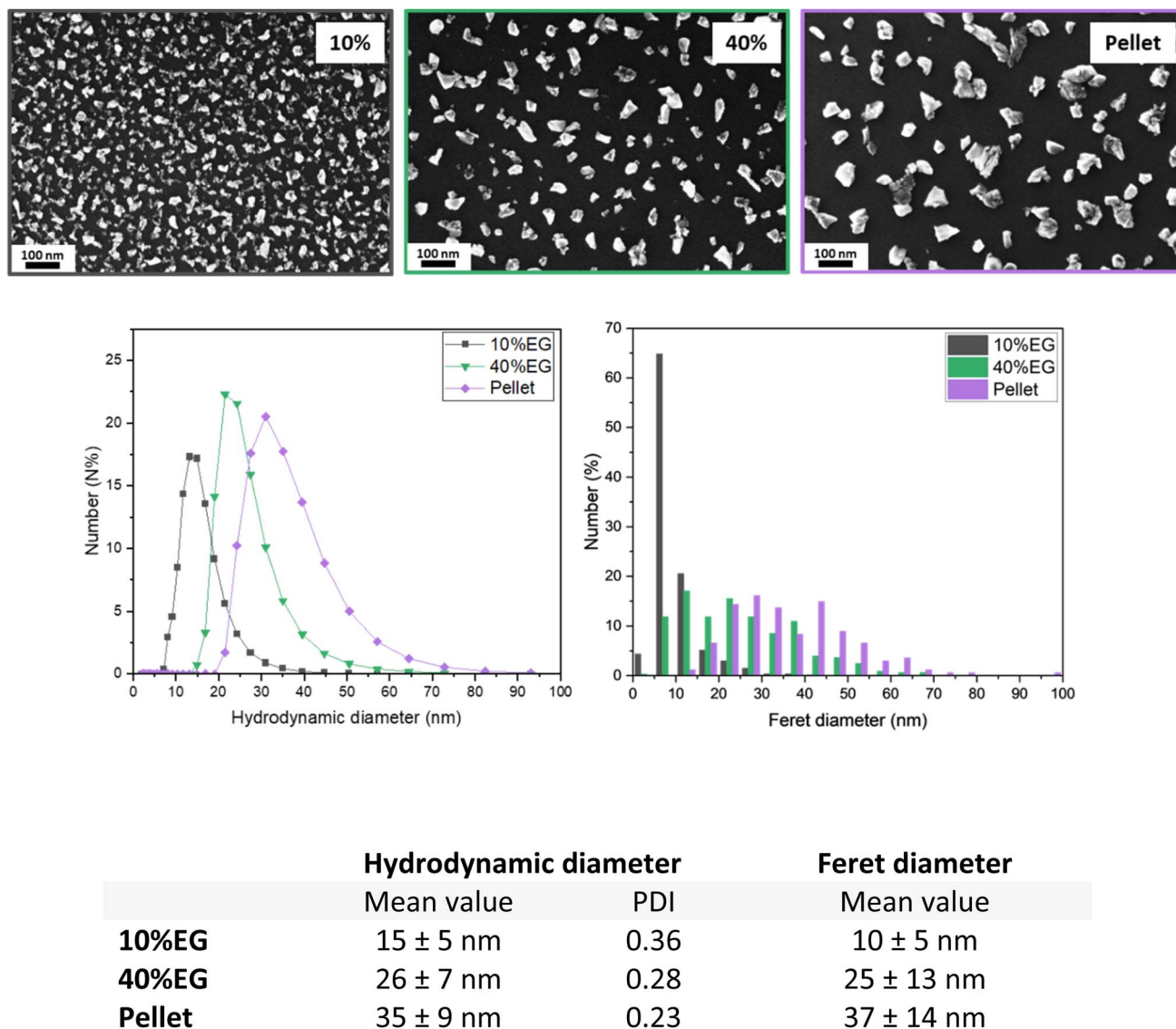|	Small tube		Large tube	
	Collected mass	% of initial mass	Collected mass	% of initial mass
10% EG	0.19 mg	5%	1.14 mg	5%
20% EG	0.29 mg	8%	1.84 mg	7%
30% EG	0.35 mg	10%	3.36 mg	13%
40% EG	0.28 mg	8%	2.67 mg	10%

Nanoscale Advances

Paper

Fig. 6 Oxidized SYP 0–0.1 nanodiamonds collected from the sediment (small tube) compared to those originating from the EG 10% and 40% gradient layers: (top) SEM pictures of the three size ranges; (bottom left) distribution of hydrodynamic diameters obtained by DLS; (bottom right) distributions of Feret diameters obtained by SEM image analysis; (bottom) table of the mean diameters and PDI. Statistics of counted MND is provided in the ESI.†

	Hydrodynamic diameter		Feret diameter
	Mean value	PDI	Mean value
10%EG	15 ± 5 nm	0.36	10 ± 5 nm
40%EG	26 ± 7 nm	0.28	25 ± 13 nm
Pellet	35 ± 9 nm	0.23	37 ± 14 nm

dimension (Table 3). Is this an intrinsic limitation of the size sorting protocol? The mass percentage of the smallest nanoparticles (<10 nm) was estimated from the initial size distribution of Ox-MND assuming a spherical shape. This diameter range corresponds to 6.4% of the initial mass. This simple calculation shows that the developed size sorting protocol aims to collect the major part of the smallest nanoparticles. To compare, amounts of small nanodiamonds collected after ultracentrifugation are at the same order of magnitude (6%).[26] However, in addition to the smallest nanoparticles, the present protocol allows the size sorting of two other size ranges compared to ultracentrifugation. Looking further at the proportions of nanoparticles sorted, we can also see that the 40% EG/H$_2$O phase represents between 8 and 10% of the initial mass, while the mass of the pellet represents at least 60% of the initial mass (considering the masses in the 50 and 60% phases

as very weak). Thus, by collecting the 10%, 40% and pellet phases, almost 75% of the initial particle mass is recovered, with the remaining 25% being lost mainly in the 20 and 30% phases, where sorting is not optimal and in the highly diluted 50 and 60% phases. Our optimal protocol results in several mg of sorted MND for each size range with the larger tube (Table 4). This is comparable to recent bottom-up approaches *via* HPHT or CVD which also provide nanodiamonds in the mg range.

A final important point to emphasize here is the accuracy of the DLS. The measurements carried out on the unsorted particles (Fig. 1) showed a certain difference between the sizes estimated by DLS and those estimated by the SEM counting. The DLS tended to overestimate the larger diameters compared to the SEM measurements. However, on the sorted phases, this difference seems to have disappeared. DLS and SEM measurements are in much better agreement (Fig. 6). Here we can see
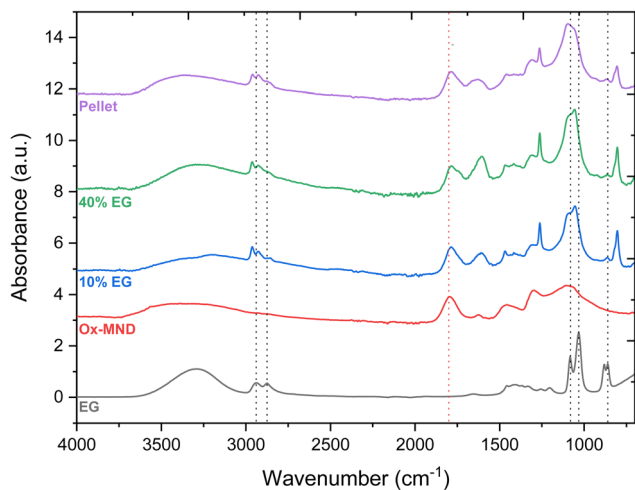
Fig. 7 Comparison of FTIR spectra for the initial oxidized MND, the size sorted ones collected from the 10% EG and 40% EG layers and pellet. An EG reference was added for comparison.

the effect of polydispersity, which particularly affects the DLS measurements. When the polydispersity is reduced, the measurements are much more reliable.

3.2 Surface chemistry of size sorted Ox-MND

The surface chemistry of size sorted MND after dialysis was investigated by FTIR and compared to the initial Ox-MND (Fig. 7). Apart from the contributions of the C–O stretching modes at 1290 cm^{-1} and 1090 cm^{-1} attributed to the anhydrous and etheric groups respectively, the IR spectrum of MND-Ox stands out for its band at 1800 cm^{-1} linked to the C=O functions.[38] This band is preserved on the sorted particles, with no obvious change in its position. Nevertheless, the spectra of the sorted particles reveal additional features, the positions of which are close to peaks visible in the EG spectrum. For example, between 2800 and 3000 cm^{-1}, the sorted MND-Ox particles reveal a band linked to C–H bonds that was absent from the initial MND-Ox particles. These C–H bonds could correspond to the CH$_2$ chains of ethylene glycol, but it is

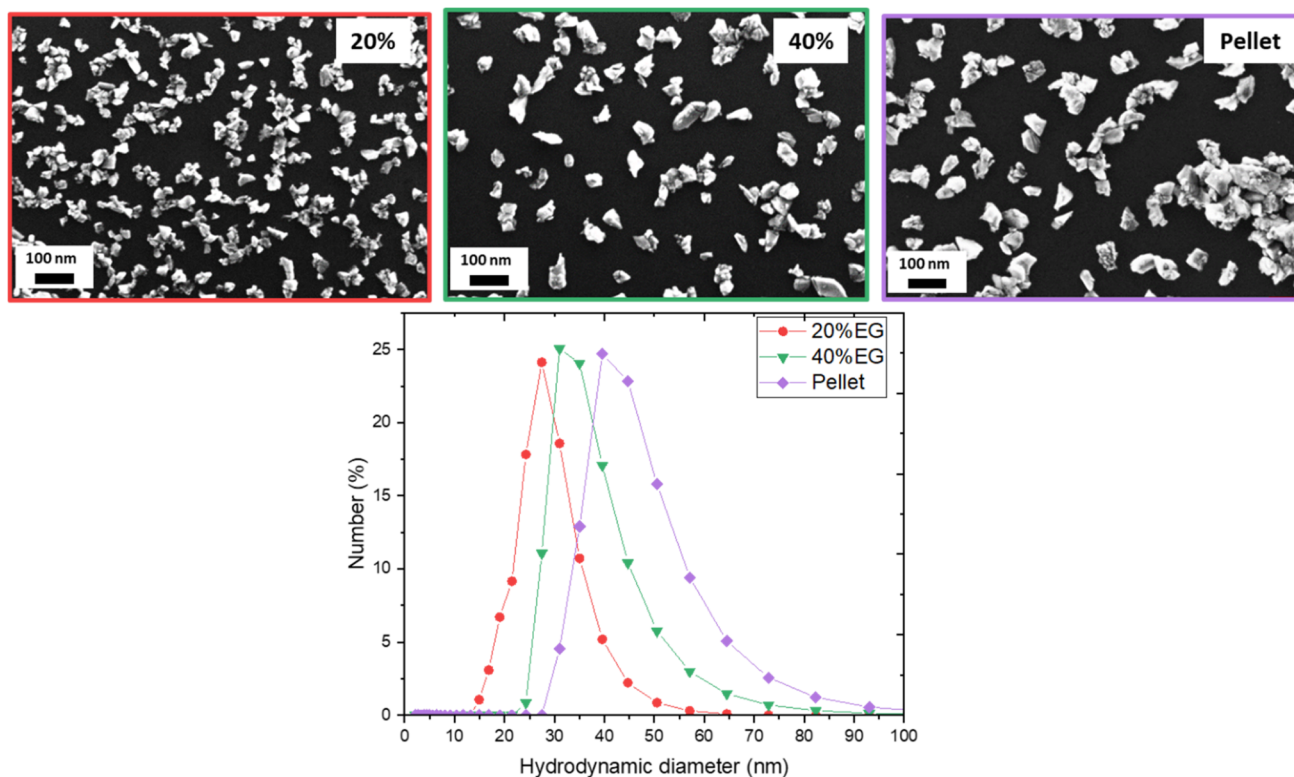|	Hydrodynamic diameter	
	Mean value	PDI
10%EG	28 ± 7 nm	0.50
40%EG	37 ± 9 nm	0.20
Pellet	46 ± 11 nm	0.21

Fig. 8 Hydrogenated SYP 0–0.1 nanodiamonds collected from the sediment (small tube) compared to those originating from the EG 20% and 40% gradient layers: (top) SEM pictures of the three size ranges; (middle) distribution of hydrodynamic diameters obtained by DLS; (bottom) table of the mean diameters and PDI.

interesting to see that the positions of these C–H stretching bonds are not identical to those of the initial EG. Similarly, it seems that the C–O stretching structure of the sorted particles is distorted compared with that of the initial particles, betraying the reminiscence of EG on the surface of the sorted particles. However, the position of the peaks is also significantly shifted. These FTIR analyses therefore seem to show that, after dialysis, a layer of EG remains adsorbed on the surface of the sorted MND-Ox, but its structure is modified by interactions, probably of the hydrogen bonding type. The quantification of this surface-adsorbed layer remains to be determined as FTIR is not an absolutely quantitative technique. This EG residue on the surface of our sorted MND-Ox is obviously undesirable, but in this study we opted for a gentle technique such as dialysis to preserve the colloidal stability of phases and make our DLS and SEM measurements more reliable. To avoid this residue, stronger purification techniques could be used, such as annealing in air, similar to that used initially to clean our MND from non-diamond phases.

3.3 Extension to hydrogenated MND

When transposing size sorting to hydrogenated MND, the behaviour of nanoparticles during sedimentation significantly changes. After centrifugation, the migration through the viscosity gradient is faster compared to oxidized nanoparticles. For the same initial mass, centrifugation velocity and duration, a highest amount of H-MND is collected in the tube pellet. Consequently, H-MND concentration collected in the 10% EG is very weak, which prevents adequate DLS measurement and accurate SEM counting. Nevertheless, for these H-MND, the smallest particles previously found in the 10% EG phase for Ox-MND were collected here in the 20% EG phase. The SEM pictures and DLS measurements of the 20% EG phase, 40% EG phase and pellet are shown in Fig. 8. Note that as H-MND behave as a positive charge when suspended in water, the layer-by-layer electrostatic deposition was achieved using an anionic polymer (PSS).[39] SEM images show that size sorting effectively occurs for H-MND. It can be seen qualitatively that the nanoparticles from the pellet are larger than those collected in the 40% EG phase, themselves larger than those from the 20% EG phase. This observation is confirmed by the DLS measurements, which show three distinct diameter ranges for each phase, with mean diameters ranging from 28 to 46 nm. However, no small isolated nanoparticles are visible in the SEM images of the 20% EG phase. In addition, it was found that H-MND do not form a monolayer as homogeneous as Ox-MND, as they tend to form small clusters, with the smallest nanoparticles adhering to the larger ones and therefore being hidden. This prevents manual counting in these SEM images. The absence of small isolated nanodiamonds can be related to the specific colloidal behavior of H-MND in water. According to previous cryo-EM investigations, hydrogenated milled nanodiamonds organize in chain-like structures up to the micron scale by facet-to-facet interactions.[40] Such chains can more easily pass through the gradient phases and quickly migrate to the bottom of the tube.
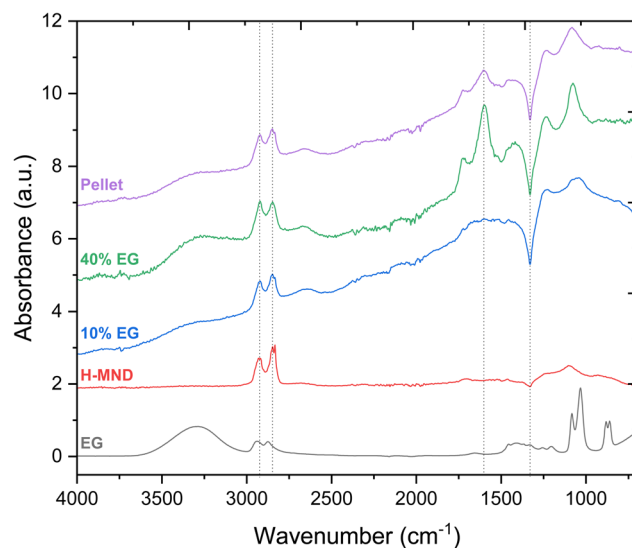

Fig. 9 Comparison of FTIR spectra for the hydrogenated MND, the size sorted ones collected from the 10% EG and 40% EG layers and pellet. An EG reference was added for comparison.

The surface chemistry of the sorted H-MND was investigated by FTIR. Looking to the corresponding spectra (Fig. 9), well-structured C–H stretching bands are observed for sorted H-MND. Their positions are in line with those of the initial H-MND. Furthermore, an absorbance dip located at 1330 cm^{-1} and a background increase are detected whatever the sorted H-MND. According to previous investigations, these features are the signature of surface conductivity, the absorbance dip being due to destructive Fano interferences.[41] This spontaneous surface conductivity of H-MND in colloidal form is becoming increasingly well documented in the literature[19,40] and appears to be related to a process similar to that observed in solid diamond, *i.e.* a transfer doping process in the presence of electron acceptor adsorbates.[42] Nevertheless, the more pronounced nature of these two signatures on sorted particles compared with the initial unsorted particles is not easy to explain at this stage, but may be due to an interaction between the nanodiamond surface and EG traces favoring transfer doping.

In the IR spectra, additional peaks compared to initial H-MND can be observed at 1050 cm^{-1} (C–O stretching modes) and 1600 cm^{-1} (not clearly assigned) for sorted larger H-MND (40% and pellet). Such peaks are either less intense (1050 cm^{-1}) or absent (1600 cm^{-1}) for the smaller population collected from the 10% EG phase. For the moment, we have no explanation for these two peaks. However, compared to sorted Ox-MND (Fig. 7), this is no clear evidence of EG residue in IR spectra. In conclusion, the sorting protocol developed in the present study can be applied to H-MND. According to IR, some specific assets of H-MND like the surface conductivity are preserved after sorting.

4. Conclusion

An efficient protocol based on an ethylene glycol/water viscosity gradient has been developed through a parametric study to sort

oxidized milled nanodiamonds by size. The combination of DLS measurements performed on aqueous suspensions and SEM counting of Ox-MND deposited layer by layer on a cationic polymer appears to be efficient in finding the right compromise in centrifugation parameters. Three size ranges can be isolated from the initial polydisperse MND in different gradient layers (10% EG, 40% EG and tube pellet). In addition to smaller sizes (<15 nm), two larger MND populations (20–60 nm range) can be separated. These three sorted phases represent up to 75% of the MND initial mass. This method appears to be very complementary to ultracentrifugation, which can isolate the smallest MND. The former protocol has been successfully extended to hydrogenated MND from the same source. Such size sorting seems very promising for MND applications, as their surface and bulk properties are strongly influenced by their size: surface reconstruction or electrostatic potentials of facets, and thermal or quantum properties. For example, it concerns the surface conductivity or the negative electron affinity specific to H-MND. Future efforts will focus on further upscaling and extension to other MND surface chemistries.

5. Materials and methods

5.1 Materials

MND particles were purchased from Van Moppes (SYP 0–0.03; SYP 0–0.05; SYP 0–0.1), while ethylene glycol, poly-dimethyldiallylammonium chloride (PDDAC) ($M_w = 100\,000 - 200\,000$ g mol^{-1}, 20 wt% in water) and poly(sodium 4-styrenesulfonate) (PSS) were purchased from Sigma-Aldrich.

5.2 Preparation of MND, Ox-MND and H-MND suspensions

Ox-MND were prepared from the as-received SYP 0–0.1, and annealed under air at 480 °C (atmospheric pressure) for 5 h. H-MND were obtained from Ox-MND, annealed under H$_2$ (atmospheric pressure, flow 50 sccm) at 750 °C for 5 h. All types of MND (as received, Ox-MND and H-MND) were suspended in ultrapure water (18.2 MΩ cm) by sonication using a Cup Horn system (Bioblock Scientific 750W) for 30 min with a 1 s on/off period (amplitude 60%). Temperature during sonication was maintained at 10 °C. Slurries of sonicated particles were then centrifuged (2400g for 40 min) and only the supernatant was kept. The centrifugation step is crucial to ensure the colloidal stability of the nanodiamond suspension and to remove any aggregates. The concentration of each suspension was estimated by weighing the dried residue of 100 μL of solution.

5.3 Viscosity gradient, phase separation and purification

In a 15 mL centrifuge tube (AstiK's), a step gradient with 2 mL phases composed of 10/90 – 20/80 – 30/70 – 40/60 – 50/50 – 60/40 (vol) EG/H$_2$O mixtures is added starting from the bottom phase with 1 mL of pure EG on the bottom of the tube (see Fig. S2†). 0.5 mL of MND suspension is added on the top of the tube. The concentration of the suspension varies between 7.4 and 7.8 mg mL^{-1} which corresponds to an initial mass of approximately 3.8 mg. The tube is centrifuged with the selected conditions and the phases are then collected using a syringe and needle,

starting with the highest phase (10%EG). For scale up, a 50 mL Falcon tube was used instead of a 15 mL Falcon tube. Step gradients were realized with 7.5 mL keeping the same EG/H$_2$O mixtures. Ethylene glycol removal is done by dialysis using a Pur-A-Lyzer Maxi dialysis kit (Sigma-Aldrich) for the 15 mL Falcon tube and a Mega dialysis kit for the 50 mL Falcon tube. Suspensions are cleaned for two days under stirring.

5.4 Dynamic light scattering (DLS) measurements

Hydrodynamic diameters were measured using a Horiba Nanopartica SZ100 system, at 25 °C with a 173° backscattering angle. Number-weighted diameter distributions and mean diameters were extracted from intensity-weighted measurements obtained by fitting the auto-correlation function with a regularized non-negative constrained least squares method, adapted to polydispersed systems. The polydispersity index was obtained from the cumulant analysis auto-correlation function. All values given here result from the average of 10 independent measurements. Previous works have underlined DLS inaccuracies occurring for too dilute suspensions. In that case, the recorded hydrodynamic diameters are overestimated,[10,43] as we also confirmed it for our MND (see Fig. S5†). For this reason, we decided to discard DLS measurements obtained for MND concentrations lower than 0.05 mg mL^{-1}.

5.5 Particle counting in SEM pictures

Monolayers of MND and Ox-MND on silicon were prepared through a layer-by-layer technique: clean 1 × 1 cm^2 silicon substrates (300 μm thick) were immersed for 20 min in a PDDAC solution (diluted by 100× from the bottle), then rinsed twice with water and directly plunged into the MND suspension for 20 min and finally rinsed twice with water. The same procedure is used for H-MND replacing PDDAC with poly(-sodium 4-styrenesulfonate) (PSS).

After being allowed to dry at ambient atmosphere and room temperature, samples were observed in a field emission scanning electron microscope (Ultra55 from Carl Zeiss, Germany). SEM pictures were realized with an acceleration voltage of 10 kV. Particle counting was realized manually, measuring the Feret diameter over at least 500 particles for each sample (using ImageJ software). Reproducibility was tested by repeating measurements on the same images (see Fig. S6†).

5.6 Estimation of the concentration of sorted suspensions by UV-vis spectroscopy

Because of the small quantities of MND collected in each phase, it was not possible to systematically measure their concentration by weighing. This is why we opted for UV-vis estimation based on their absorption at 300 nm. UV-vis spectra were acquired on a Shimadzu UV-3600 Plus series with a quartz cell with an optical pathway of 1 cm. A calibration curve was realized with the absorption values at 300 nm of 8 suspensions of Ox-MND at different concentrations (see Fig. S7†). We are aware of the limitations of this method on polydispersed nano-diamonds for which a strong influence of nanoparticle diameter due to Rayleigh scattering is expected. In order to estimate the

influence of this bias, we compared the values measured by UV-vis and by weighing (by drying large quantities to obtain a significant value) on certain samples. For the largest nanoparticles, we measured an error of less than 10% on the value, while for the smallest particles, this error rises up to 30% with an underestimation by UV-vis. Nevertheless, while this error is not negligible, in our opinion, it does not call into question the results obtained previously.

5.7 Infrared spectroscopy

Fourier Transform Infrared Spectroscopy was performed on a Bruker Alpha II spectrometer equipped with a Platinum ATR system. For each measurement, 4 μL of MND in suspension were dried on the crystal under a dry nitrogen flow (1 L min^{-1}). Spectra acquisition was realized while maintaining the nitrogen flow. The spectra represented here are the average of 128 scans, with a resolution of 4 cm^{-1}.

Data availability

All data generated or analyzed during this study are included in this article and in the ESI†.

Conflicts of interest

There are no conflicts to declare.

Acknowledgements

References

1 J. Xu and E. K. H. Chow, *SLAS Technol.*, 2023, **28**, 214–222.

2 X. W. Gao, Z. W. Zhao, Y. He, S. F. Fan, K. R. Jiao, S. Y. Lou, X. Y. Han, P. F. Song, R. Cai, Z. Hu, Z. J. Jiang, Y. J. Wang and J. Q. Zhu, Nanodiamond: a promising metal-free nanoscale material in photocatalysis and electrocatalysis, *Trans. Nonferrous Met. Soc. China*, 2024, **43**, 3501–3552.

3 X. Wang, J. Xu, S. Ge, L. Zou, D. Sang, J. Fan and Q. Wang, *APL Mater.*, 2023, **11**, 090603.

4 J.-C. Arnault, *Nanodiamonds*, Elsevier, 2017.

5 H. A. Girard and J.-C. Arnault, in *Tuning surface properties of detonation and milled nanodiamonds by gas phase modifications*, ed. S. Mandal and N. Yang, Springer Nature Switzerland Cham, 2024, pp. 47–76.

6 D. Miliaieva, A. S. Djoumessi, J. Čermák, K. Kolářová, M. Schaal, F. Otto, E. Shagieva, O. Romanyuk, J. Pangrác, J. Kuliček, V. Nádaždy, S. Stehlik, A. Kromka, H. Hoppe and B. Rezek, *Nanoscale Adv.*, 2023, **5**, 4402–4414.

7 J. Tisler, G. Balasubramanian, B. Naydenov, R. Kolesov, B. Grotz, R. Reuter, J. P. Boudou, P. A. Curmi, M. Sennour, A. Thorel, M. Börsch, K. Aulenbacher, R. Erdmann, P. R. Hemmer, F. Jelezko and J. Wrachtrup, *ACS Nano*, 2009, **3**, 1959–1965.

8 N. Nunn, M. Torelli, G. McGuire and O. Shenderova, *Curr. Opin. Solid State Mater. Sci.*, 2017, **21**, 1–9.

9 N. Nunn, N. Prabhakar, P. Reineck, V. Magidson, E. Kamiya, W. F. Heinz, M. D. Torelli, J. Rosenholm, A. Zaitsev and O. Shenderova, *Nanoscale*, 2019, **11**, 11584–11595.

10 S. Stehlik, M. Mermoux, B. Schummer, O. Vanek, K. Kolarova, P. Stenclova, A. Vlk, M. Ledinsky, R. Pfeifer, O. Romanyuk, I. Gordeev, F. Roussel-Dherbey, Z. Nemeckova, J. Henych, P. Bezdicka, A. Kromka and B. Rezek, *J. Phys. Chem. C*, 2021, **125**, 5647–5669.

11 S. Sotoma, C. P. Epperla and H. C. Chang, *ChemNanoMat*, 2018, **4**, 15–27.

12 K. Turcheniuk and V. N. Mochalin, *Nanotechnology*, 2017, **28**, 252001.

13 I. Rehor and P. Cigler, *Diam. Relat. Mater.*, 2014, **46**, 21–24.

14 O. A. Shenderova and G. E. McGuire, *Biointerphases*, 2015, **10**, 030802.

15 J. Y. Raty, G. Galli, C. Bostedt, T. W. Van Buuren and L. J. Terminello, *Phys. Rev. Lett.*, 2003, **90**, 1–4.

16 S. L. Y. Chang, C. Dwyer, E. Osawa and A. S. Barnard, *Nanoscale Horiz.*, 2018, **3**, 213–217.

17 H. Matsubara, G. Kikugawa, T. Bessho and T. Ohara, *Diam. Relat. Mater.*, 2020, **102**, 107669.

18 A. S. Barnard and E. O'Sawa, *Nanoscale*, 2014, **6**, 1188–1194.

19 S. Stehlik, O. Szabo, E. Shagieva, D. Miliaieva, A. Kromka, Z. Nemeckova, J. Henych, J. Kozempel, E. Ekimov and B. Rezek, *Carbon Trends*, 2024, **14**, 100327.

20 W. Li, N. Mingo, L. Lindsay, D. A. Broido, D. A. Stewart and N. A. Katcho, *Phys. Rev. B: Condens. Matter Mater. Phys.*, 2012, **85**, 1–5.

21 A. S. Barnard, *Cryst. Growth Des.*, 2009, **9**, 4860–4863.

22 T. Yuan and K. Larsson, *J. Phys. Chem. C*, 2014, **118**, 26061–26069.

23 E. A. Ekimov, O. S. Kudryavtsev, A. A. Khomich, O. I. Lebedev, T. A. Dolenko and I. I. Vlasov, *Adv. Mater.*, 2015, **27**, 5518–5522.

24 M. De Feudis, A. Tallaire, L. Nicolas, O. Brinza, P. Goldner, G. Hétet, F. Bénédic and J. Achard, *Adv. Mater. Interfaces*, 2020, **7**, 1–7.

25 P. Li, A. Kumar, J. Ma, Y. Kuang, L. Luo and X. Sun, *Sci. Bull.*, 2018, **63**, 645–662.

26 Y. Morita, T. Takimoto, H. Yamanaka, K. Kumekawa, S. Marino, S. Aonuma, T. Kimura and N. Komatsu, *Small*, 2008, **4**, 2154–2157.

27 S. V. Koniakhin, N. A. Besedina, D. A. Kirilenko, A. V. Shvidchenko and E. D. Eidelman, *Superlattices Microstruct.*, 2018, **113**, 204–212.

28 P. Qiu and C. Mao, *Adv. Mater.*, 2011, **23**, 4880–4885.

29 F. Bonaccorso, M. Zerbetto, A. C. Ferrari and V. Amendola, *J. Phys. Chem. C*, 2013, **117**, 13217–13229.

30 C. S. Bhatt, B. Nagaraj, D. Ghosh, S. Ramasamy, R. Thapa, S. B. Marpu and A. K. Suresh, *Soft Matter*, 2019, **15**, 7787–7794.

31 Y. Asnaashari Kahnouji, E. Mosaddegh and M. A. Bolorizadeh, *Mater. Sci. Eng., C*, 2019, **103**, 109817.

32 R. Mahfouz, D. L. Floyd, W. Peng, J. T. Choy, M. Loncar and O. M. Bakr, *Nanoscale*, 2013, **5**, 11776–11782.

33 W. Peng, R. Mahfouz, J. Pan, Y. Hou, P. M. Beaujuge and O. M. Bakr, *Nanoscale*, 2013, **5**, 5017–5026.

34 J. Qu, J. F. Mukerabigwi, N. Yang, X. Huang, Y. Sun, X. Cai and Y. Cao, *Appl. Nanosci.*, 2021, **11**, 257–266.

35 H. A. Girard, S. Perruchas, C. Gesset, M. Chaigneau, L. Vieille, J.-C. Arnault, P. Bergonzo, J.-P. Boilot and T. Gacoin, *ACS Appl. Mater. Interfaces*, 2009, **1**, 2738–2746.

36 K. Henni, C. Njel, M. Frégnaux, D. Aureau, J. S. Mérot, F. Fossard, I. Stenger, J. C. Arnault and H. A. Girard, *Diam. Relat. Mater.*, 2024, **142**, 110770.

37 *Particle Size Analysis—Dynamic Light Scattering (DLS) ISO 22412:2017*, 2017.

38 T. Petit and L. Puskar, *Diam. Relat. Mater.*, 2018, **89**, 52–66.

39 M. Couty, H. A. Girard and S. Saada, *ACS Appl. Mater. Interfaces*, 2015, **7**, 15752–15764.

40 L. Saoudi, H. A. Girard, E. Larquet, M. Mermoux, J. Leroy and J. C. Arnault, *Carbon*, 2023, **202**, 438–449.

41 O. S. Kudryavtsev, R. H. Bagramov, A. M. Satanin, A. A. Shiryaev, O. I. Lebedev, A. M. Romshin, D. G. Pasternak, A. V. Nikolaev, V. P. Filonenko and I. I. Vlasov, *Nano Lett.*, 2022, **22**, 2589–2594.

42 F. Maier, M. Riedel, B. Mantel, J. Ristein and L. Ley, *Phys. Rev. Lett.*, 2000, **85**, 3472–3475.

43 R. Tantra, P. Schulze and P. Quincey, *Particuology*, 2010, **8**, 279–285.